We are IntechOpen, the world's leading publisher of Open Access books Built by scientists, for scientists

4,800
Open access books available

122,000
International authors and editors

135M
Downloads

Our authors are among the

154
Countries delivered to

TOP 1%
most cited scientists

12.2%
Contributors from top 500 universities

CLARIVATE ANALYTICS
BOOK CITATION INDEX
INDEXED

WEB OF SCIENCE™

Selection of our books indexed in the Book Citation Index
in Web of Science™ Core Collection (BKCI)

Interested in publishing with us?
Contact book.department@intechopen.com

Fabrication and Characterization of Element-Doped Perovskite Solar Cells

Takeo Oku, Masahito Zushi, Kohei Suzuki,

Yuya Ohishi, Taisuke Matsumoto and Atsushi Suzuki

Additional information is available at the end of the chapter

Abstract

Perovskite solar cells were fabricated and characterized. X-ray diffraction analysis and transmission electron microscopy were used for investigation of the devices. The structure analysis by them showed structural transformation of the crystal structure of the perovskite, which indicated that a cubic-tetragonal crystal system depended on the annealing condition. The photovoltaic properties of the cells also depended on the structures. Metal doping and halogen doping to the perovskite and TiO_2 were also investigated. The results showed an increase in the efficiencies of the devices, due to the structural change of the perovskite compound layers.

Keywords: perovskite, solar cell, doping, structure, $CH_3NH_3PbI_3$, Sb, Cl, TiO_2, Nb, Ge, Cs

1. Introduction

Various organic-inorganic hybrid solar cells with perovskite-type pigments have been broadly studied recently [1–4]. Organic solar cells with a $CH_3NH_3PbI_3$ compound that has a perovskite structure have high conversion efficiencies [5–7]. Since achieving a photoconversion efficiency of 15% [8], higher efficiencies have been reported for various device structures and processes [9–11], and the photoconversion efficiency increased up to ca. 20% [12–18]. The solar cell properties depend on the crystal structures of the perovskite phase, electron transport layers, hole transport layers (HTLs), nanoporous layers, and fabrication process. Especially, the energy band gaps and carrier transport of the perovskite compounds are dependent on the crystal structures [19], and further analyses of the structures and properties are imperative.

In this article, fabrication and characterization of perovskite-type solar cells are reviewed and summarized. Various perovskite compounds, such as $CH_3NH_3PbI_3$, $[HC(NH_2)_2]PbI_3$, and $CsSnI_3$, are expected for solar cell materials. Since these perovskite-type materials often have nanostructures in the solar cell devices, information on the crystal structures, fabrication, and characterization would be useful for fabrication of the perovskite-type crystals. Transmission electron microscopy, electron diffraction, and high-resolution electron microscopy are powerful tools for structure analysis of solar cells [20] and perovskite-type structures in atomic scale [21–23].

The crystals of $CH_3NH_3PbX_3$ ($X = Cl$, Br, or I) have perovskite structures and provide structural transitions upon heating [24–26]. The crystal structures of cubic, tetragonal, and orthorhombic $CH_3NH_3PbI_3$ are shown in **Figure 1(a)–(c)**, respectively. Space group is *Pm-3m*, and the lattice constant $a = 6.391$ Å at 330 K for cubic $CH_3NH_3PbI_3$ [27]. Hydrogen positions in the orthorhombic $CH_3NH_3PbI_3$ were also determined at 4 K by neutron diffraction [28], as shown in **Figure 1(d)**. Although the crystals of perovskite $CH_3NH_3PbX_3$ provide a cubic system as the high-temperature phase, the $CH_3NH_3^+$ ions are polar and have a symmetry of C_{3v}. This results in formation of cubic phase with disordering [27]. Besides the $CH_3NH_3^+$ ions, disordering of the halogen ions is also observed in the cubic perovskite phase, as indicated in **Figure 1(a)**. Site occupancies of I were 1/4, and those of C and N were 1/12, respectively. The CH_3NH_3 ion occupies 12 equivalent orientations of the C_2 axis, and hydrogen atoms have two kinds of configurations on the C_2 axis. Therefore, the total degree of freedom is 24 [26].
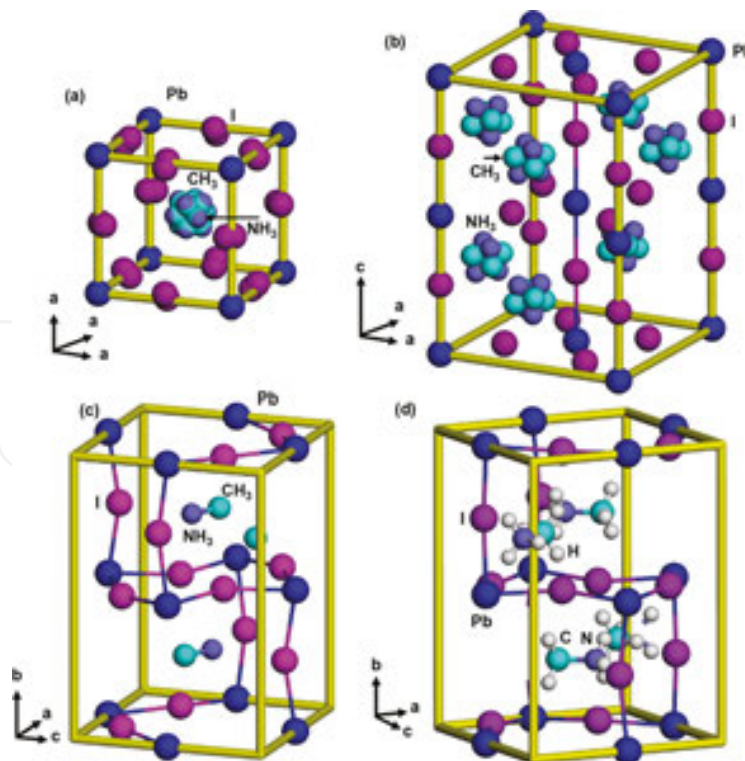

Figure 1. Structure models of $CH_3NH_3PbI_3$ with (a) cubic, (b) tetragonal and (c) orthorhombic structures, and (d) orthorhombic $CH_3NH_3PbI_3$ with hydrogen positions.

In addition to the $CH_3NH_3PbI_3$ (MAPbI$_3$), [HC(NH$_2$)$_2$]PbI$_3$ (formamidinium lead iodide, FAPbI$_3$) provided high conversion efficiencies [17, 18]. Structure parameters, including hydrogen positions, were also determined at 298 K by neutron diffraction [29], and the structure model with the lattice constant a = 6.3620 Å is shown in **Figure 2(a)**.

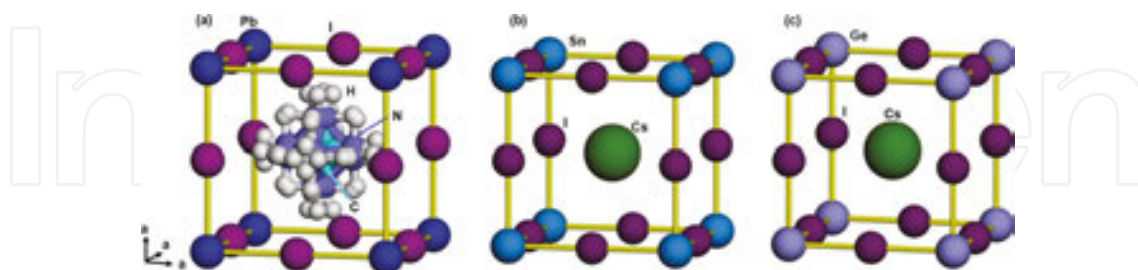**Figure 2.** Structure models of (a) [HC(NH$_2$)$_2$]PbI$_3$, (b) CsSnI$_3$, and (c) CsGeI$_3$ with cubic structures.

CH_3NH_3 ions can be substituted by other elements such as Cs. The structure models of CsSnI$_3$ and CsGeI$_3$ for high-temperature phase are shown in **Figure 2(b)** and **(c)**, respectively [30–32]. Space group is *Pm-3m* (Z = 1), and a = 6.219 Å at 446 K for CsSnI$_3$, a = 6.05 Å at 573 K for CsGeI$_3$, respectively. Solar cells with F-doped CsSnI$_{2.95}$F$_{0.05}$ provided a photoconversion efficiency of 8.5% [6].

2. Basic device structures

A typical fabrication process of the TiO$_2$/CH$_3$NH$_3$PbI$_3$ photovoltaic devices is described here [8, 33, 34]. Fluorine-doped tin oxide (FTO) substrates were washed in an ultrasonic cleaner using methanol and acetone, and then dried in N$_2$ gas. Precursor solution of 0.30 M TiO$_x$ was prepared from titanium diisopropoxide bis(acetyl acetonate) with 1-butanol, and the TiO$_x$ precursor solution was spin-coated on the FTO substrate at 3000 rpm and annealed at 125°C for 5 min. This process was carried out two times, and the FTO substrate was annealed at 500°C for 30 min to form the compact TiO$_2$ layer as an electron transport layer. After that, TiO$_2$ paste was coated on the substrate by a spin-coating method at 5000 rpm to form a mesoporous structure. For the mesoporous TiO$_2$ layer, TiO$_2$ paste was arranged with TiO$_2$ powder with poly(ethylene glycol) in ultrapure water. The solution was stirred with triton X-100 and acetylacetone for 30 min. The prepared cells were heated at 120°C, and annealed at 500°C for 30 min in air. Designed for the preparation of pigment with a perovskite structure, a solution of CH$_3$NH$_3$I and PbI$_2$ with a mole ratio of 1:1 in γ-butyrolactone was mixed at 60°C. The mixture solution of CH$_3$NH$_3$I and PbI$_2$ was then poured into the TiO$_2$ mesopores by spin-coating, and annealed at 100°C. After that, the hole transport layer (HTL) was prepared by the spin coating. For preparation of the HTL, a solution of spiro-OMeTAD in chlorobenzene was mixed with a solution of lithium bis(trifluoromethylsulfonyl) imide (Li-TFSI) in acetonitrile for 12 h. The former solution with 4-tert-butylpyridine was mixed with the Li-TFSI solution at 70°C. Finally, gold (Au) metal contacts were evaporated as top electrodes of the cell. Layered structures of

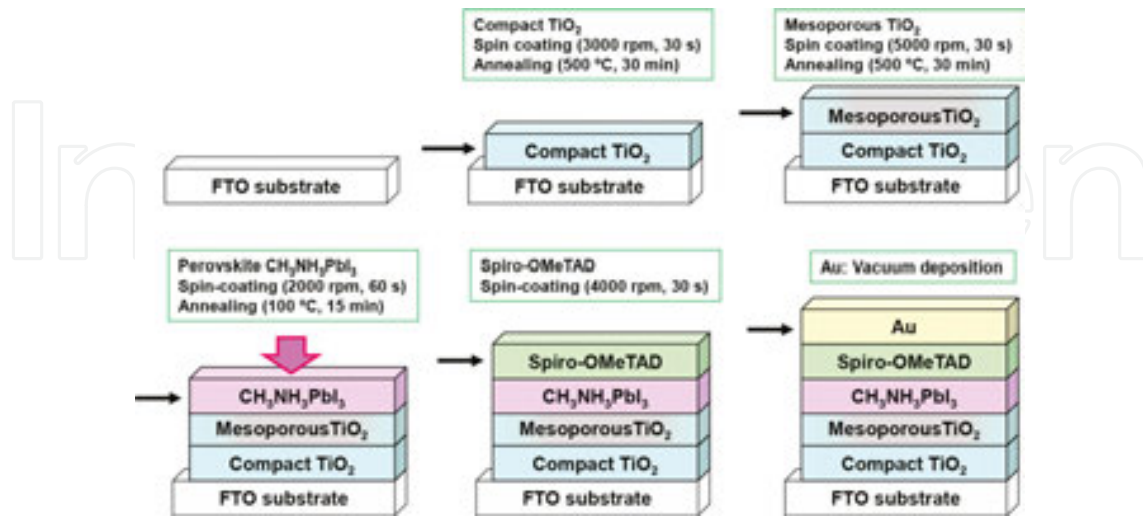the present photovoltaic cells were represented as FTO/TiO$_2$/CH$_3$NH$_3$PbI$_3$/Spiro-OMeTAD/Au, as shown in **Figure 3**.

Figure 3. Schematic illustration for the fabrication of CH$_3$NH$_3$PbI$_3$ photovoltaic cells.

The typical *J–V* characteristics of the TiO$_2$/CH$_3$NH$_3$PbI$_3$/spiro-OMeTAD photovoltaic cells under illumination are shown in **Figure 4(a)**, which indicates an annealing effect of the CH$_3$NH$_3$PbI$_3$ layer. The as-deposited CH$_3$NH$_3$PbI$_3$ cell provided a conversion efficiency of 2.83%. The CH$_3$NH$_3$PbI$_3$ cell annealed at 100°C for 15 min provided better photovoltaic properties compared with the as-deposited one, as shown in **Figure 4(a)**. The highest efficiency was obtained for the annealed CH$_3$NH$_3$PbI$_3$ cell, which provided a power conversion efficiency of 5.16%, a fill factor of 0.486, a short-circuit current density of 12.9 mA cm^{-2}, and an open-
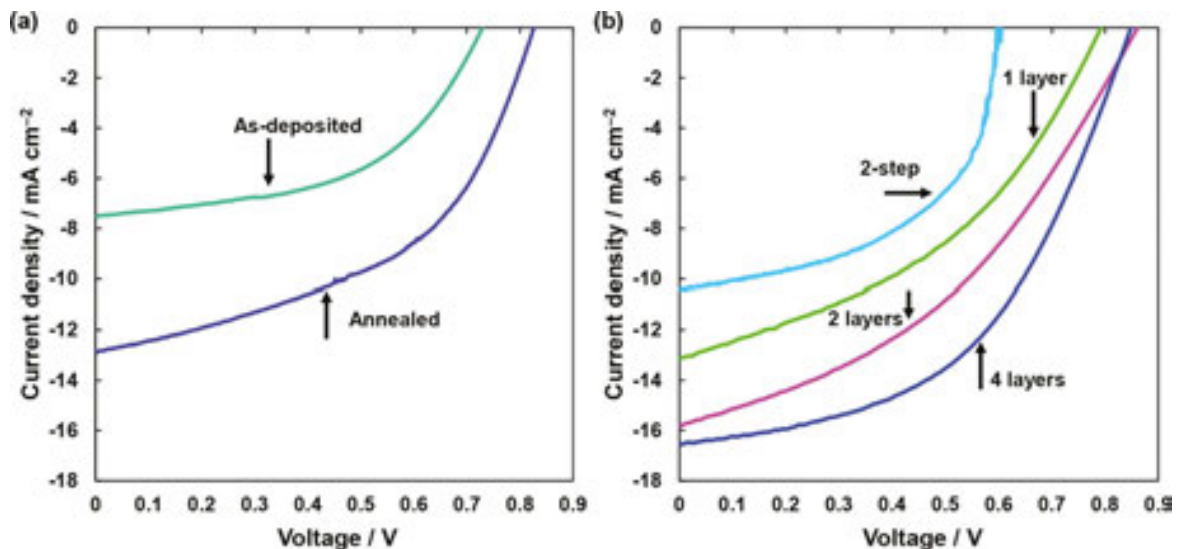

Figure 4. *J–V* characteristics of TiO$_2$/CH$_3$NH$_3$PbI$_3$ photovoltaic cells. (a) As-deposited and annealed samples. (b) CH$_3$NH$_3$PbI$_3$ layers prepared by multiple spin-coating.

circuit voltage of 0.827 V [35]. **Figure 4(b)** shows results of multiple spin-coating of $CH_3NH_3PbI_3$, which will be described later.

XRD patterns of $CH_3NH_3PbI_3$ thin films on the glass substrate are shown in **Figure 5(a)**. The diffraction reflections could be indexed with tetragonal and cubic structures for as-deposited and annealed films, respectively. Though the as-deposited film showed a single phase of the perovskite structure, broader diffraction reflections owing to a PbI_2 phase appeared after annealing, as shown in **Figure 5(a)**. **Figure 5(b)** and **(c)** is enlarged XRD patterns at 2θ of ~14° and ~28°, respectively. Split diffraction reflections of 002–110 and 004–220 for the as-deposited sample changed into diffraction reflections of 100 and 200 after annealing, which indicate the
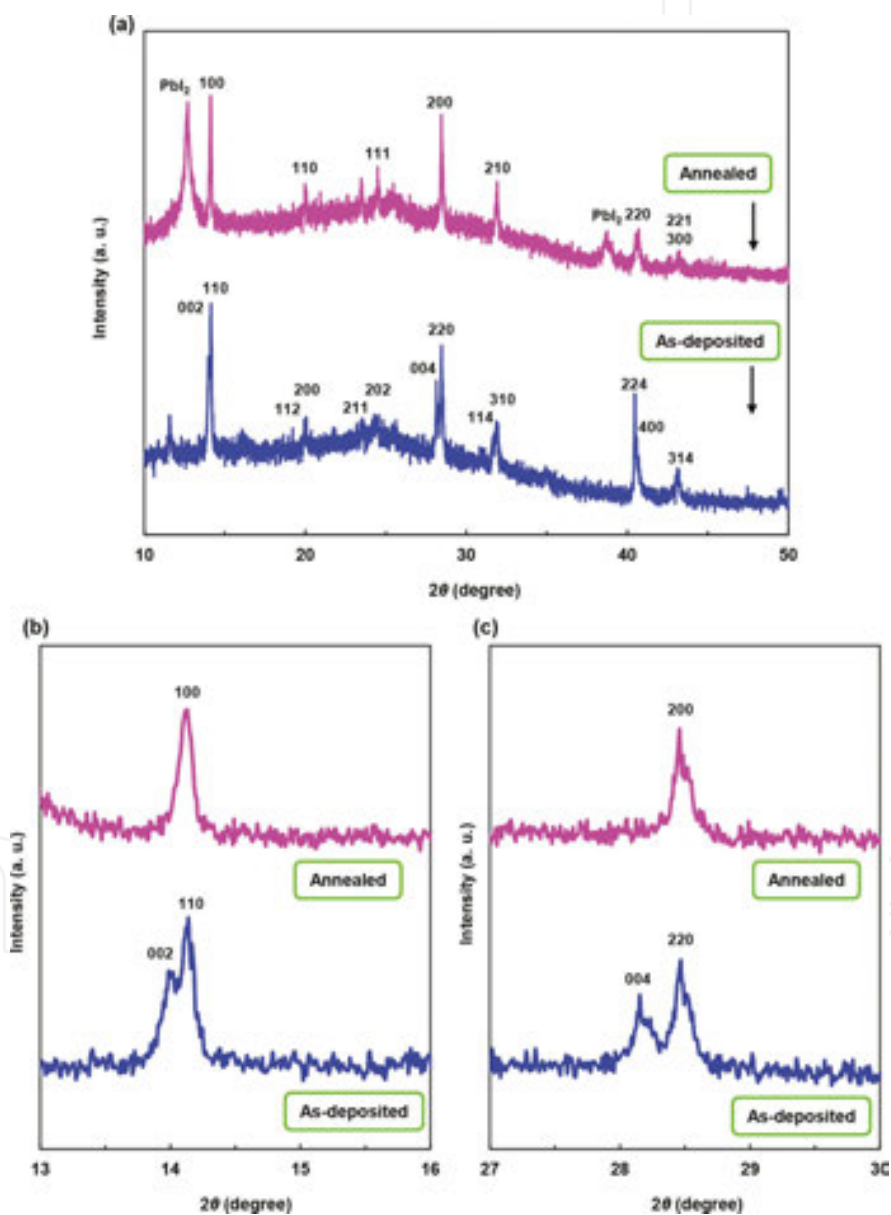

Figure 5. (a) XRD patterns of $CH_3NH_3PbI_3$ thin films before and after annealing. Enlarged XRD patterns at 2θ of (b) ~14° and (c) ~28°.

structural transformation from the tetragonal to cubic system. The $CH_3NH_3PbI_3$ crystals have perovskite structures and provide structural transitions from a tetragonal to a cubic system upon heating at ~330 K, as shown in the structure models of **Figure 1(a)** and **(b)**. For the high-temperature phase, unit cell volume of the cubic system is 261 Å³, which is bigger compared with that of the tetragonal system (246 Å³), as shown in **Table 1** [35]. This might be because of both thermal expansion of the unit cell and atomic disordering of iodine in the cubic structure. As the temperature decreases, the tetragonal structure is transformed to the orthorhombic structure because of ordering of CH_3NH_3 ions in the unit cell [37].

Samples	Crystal system	Lattice constants (Å)	V (Å³)	Z	V/Z (Å³)
As-deposited	Tetragonal	a = 8.8620	993.10	4	248.27
		c = 12.6453			
Annealed	Cubic	a = 6.2724	246.78	1	246.78
Ref. [36] (220 K)	Tetragonal	a = 8.800	982.33	4	245.6
		c = 12.685			
Ref. [27] (330 K)	Cubic	a = 6.391	261.0	1	261.0

V: unit cell volume; Z: number of chemical units in the unit cell.

Table 1. Measured and reported structural parameters of $CH_3NH_3PbI_3$.

The XRD results in **Figure 5** indicated phase transformation of the $CH_3NH_3PbI_3$ perovskite structure from the tetragonal to the cubic system by partial separation of PbI_2 from the $CH_3NH_3PbI_3$ phase at elevated temperatures, which would be related to the decrease of the unit cell volume of the perovskite structure from 248.3 to 246.8 Å³, as shown in **Table 1**. Besides the iodine atoms, Pb atoms may be deficient, and the occupancy of the Pb sites might be smaller than 1. It should be noted that the structural transition of the $CH_3NH_3PbI_3$ from the tetragonal to cubic system here would be attributed to the formation of PbI_2 by decomposition of the $CH_3NH_3PbI_3$ phase, which is different from the ordinary tetragonal-cubic transition at 330 K [24, 25].

Figure 6(a) and **(b)** is the TEM image and the electron diffraction pattern of TiO_2/$CH_3NH_3PbI_3$, respectively [35]. The TEM image shows TiO_2 nanoparticles with sizes of ~50 nm, and the polycrystalline $CH_3NH_3PbI_3$ phase shows dark contrast, which is due to Pb having the largest atomic number in the present materials.

The electron diffraction pattern of **Figure 6(b)** shows the Debye-Scherrer rings from the nanocrystalline TiO_2 particles, which can be indexed with the 101, 004, and 200 reflections of anatase-type TiO_2. Thickness of the mesoporous TiO_2 layer was found to be ~300 nm from atomic force microscopy measurements. Along with the Debye–Scherrer rings of TiO_2, diffraction reflections agreeing with the $CH_3NH_3PbI_3$ structure [6] were observed and indexed, as shown in **Figure 6(b)**. Other diffraction spots, except for the Debye-Scherrer rings of TiO_2, are also from the $CH_3NH_3PbI_3$ nanoparticles. A structure model and its calculated electron diffraction pattern of a cubic $CH_3NH_3PbI_3$ phase projected along the [210] direction are shown

in **Figure 6(c)** and **(d)**, respectively. The calculated electron diffraction pattern agrees well with the observed pattern of **Figure 6(b)**.
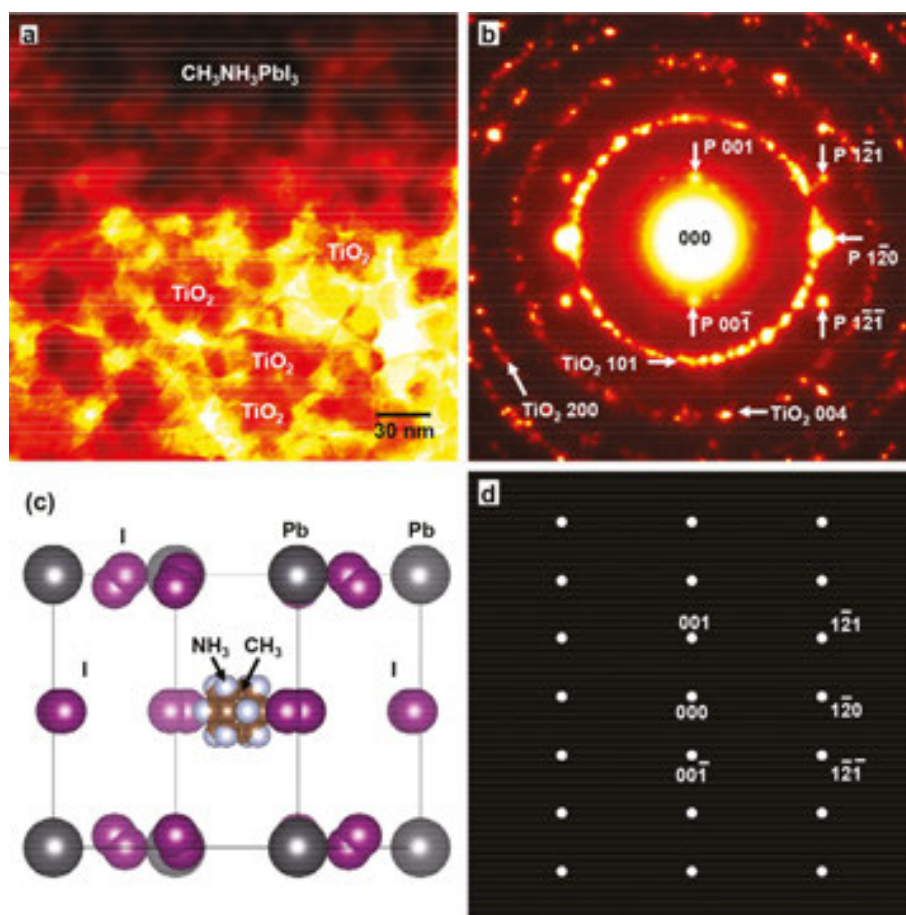

Figure 6. (a) TEM image and (b) electron diffraction pattern of $TiO_2/CH_3NH_3PbI_3$. "P" indicates $CH_3NH_3PbI_3$ perovskite phase. (c) Structure model and (d) its calculated electron diffraction pattern of cubic $CH_3NH_3PbI_3$ projected along the [210] direction.

Figure 7(a) is a high-resolution TEM image of the $CH_3NH_3PbI_3$ taken along the a-axis [33]. The images of thinner parts of the crystals indicate the direct projection of the crystal structure [21, 22]. The darkness and the size of the dark spots corresponding to Pb positions could be directly identified, and atomic positions of iodine (I) in the crystal indicate weak contrast, as compared with the projected atomic structure model of $CH_3NH_3PbI_3$ along the [100] direction in **Figure 7(b)**. NH_3 and CH_3 molecules cannot be represented as dark spots in the image, which is due to the smaller atomic number of N and C. **Figure 7(c)** is a high-resolution image of the surface of a TiO_2 nanoparticle, which indicates {101} lattice fringes.

The J–V characteristics of the $TiO_2/CH_3NH_3PbI_3$/spiro-OMeTAD photovoltaic cells prepared by multiple spin-coating of $CH_3NH_3PbI_3$ are shown in **Figure 4(b)**. **Figure 4(b)** indicates the effect of spin-coating times of $CH_3NH_3PbI_3$ on the photovoltaic properties. The highest efficiency of 6.96% was achieved for the cell coated for four times, which provided a J_{SC} of 16.5 mA cm^{-2}, a V_{OC} of 0.848 V, and FF of 0.496. More spin-coating reduced the efficiencies of the

cells. Although 2-step deposition [8] (spin-coating PbI_2 and dipping in the CH_3NH_3I solution) was also performed in air, the efficiency was lower compared with that by multiple spin-coating, as observed in **Figure 4(b)**. It is believed that the $CH_3NH_3PbI_3$ phase was embedded inside pores of the mesoporous TiO_2 layer during one- or two-time spin-coating. After the inside pores of the mesoporous TiO_2 were completely filled with the perovskite compound, only the perovskite layer might be formed on the mesoporous TiO_2 layer by four-time spin-coating, which would result in the highest efficiency.
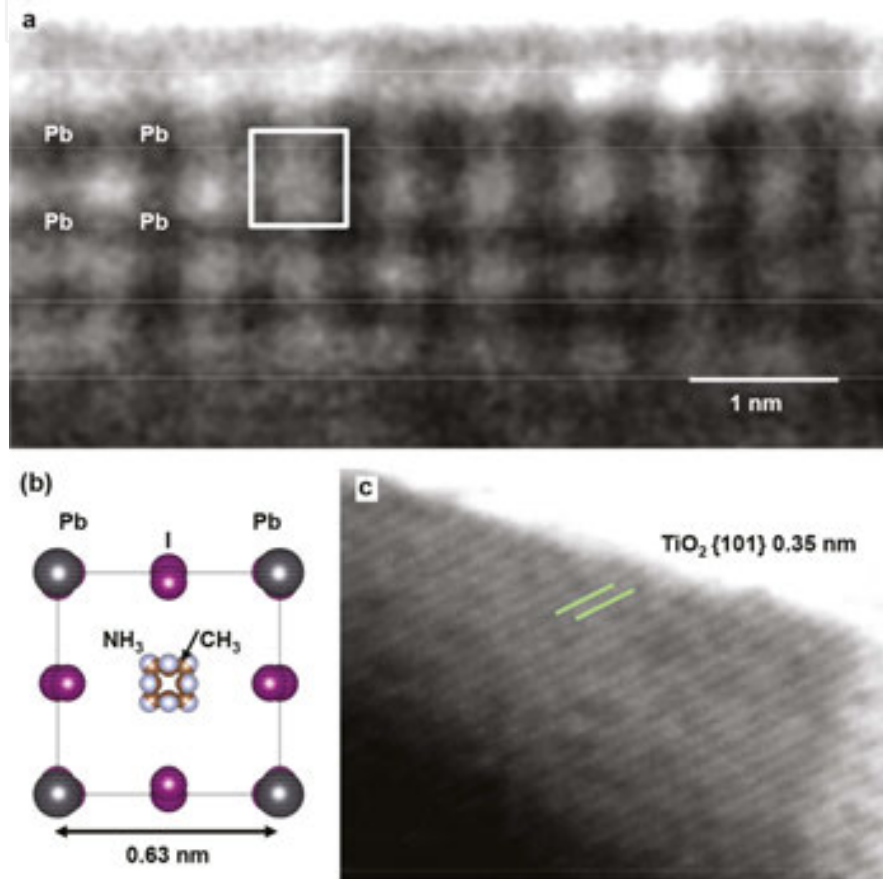

Figure 7. (a) High-resolution TEM image and (b) structure model of $CH_3NH_3PbI_3$. (c) Lattice image of TiO_2.

The IPCE spectrum of the photovoltaic cell with the $TiO_2/CH_3NH_3PbI_3$/spiro-OMeTAD structure exhibits photoconversion efficiencies between 300 and 800 nm, which nearly agrees with the measured energy gaps of 1.51 eV [37] for the $CH_3NH_3PbI_3$ compound. This indicates that excitons might be effectively generated in the perovskite compound layers upon light illumination.

An energy level diagram of $TiO_2/CH_3NH_3PbI_3$ photovoltaic cells is summarized as shown in **Figure 8(a)**. The electronic charge generation is caused by light irradiation from the FTO substrate side. The TiO_2 layer receives the electrons from the $CH_3NH_3PbI_3$ crystal, and the electrons are carried to the FTO. On the other hand, the holes are carried to the Au electrode through the HTL of spiro-OMeTAD. For these processes, the devices were produced in air,

which would induce the reduction of device stability. Perovskite compounds with higher crystal quality would be produced in future works.
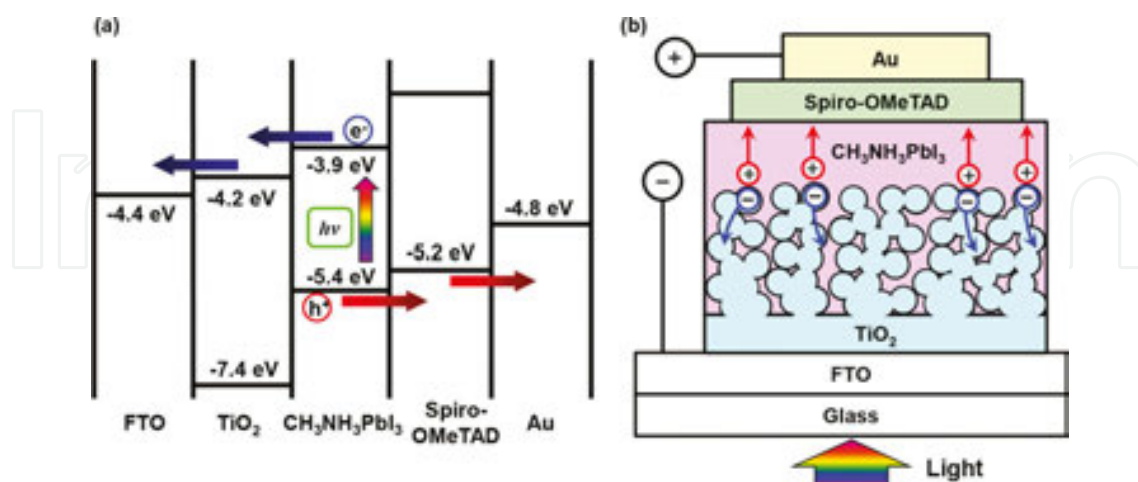

Figure 8. (a) IPCE spectrum and (b) energy level diagram of $TiO_2/CH_3NH_3PbI_3$ cell. (c) Model of interfacial structure.

From the TEM results, size distributions of TiO_2 nanoparticles were observed, indicating a microcrystalline structure, as shown in **Figure 6(b)**, and there seems to be no special crystallographic relation at the interface. The interface between the TiO_2 and $CH_3NH_3PbI_3$ phases would not be perfectly connected over the large area. The cell prepared by four-time spincoating provided the highest efficiency, which would have an interfacial microstructure as shown in **Figure 8(b)**. The layer thickness of the $CH_3NH_3PbI_3$ phase was too thick for the cells prepared by 10-time spin-coating, which resulted in an increase in the inner electronic resistance and decrease in the efficiency.

As a summary, the structure analysis of $TiO_2/CH_3NH_3PbI_3$ indicated phase transformation of the perovskite structure from the tetragonal to the cubic system by partial separation of PbI_2 from the $CH_3NH_3PbI_3$ compound upon annealing, which was presumed by decrease of the unit cell volume of the perovskite structure and resulted in the enhancement of photovoltaic properties of the devices. Effects of the multiple spin-coating were also investigated, which improved the efficiency when the four-time spin-coating was carried out. The improvement of the devices might attribute to the complete coverage and optimal thickness of the perovskite layer on the porous TiO_2. Additionally, the lattice constants and crystallite sizes of the $CH_3NH_3PbI_3$ increased and decreased, respectively, which indicates the microstructural difference of the perovskite phase between the inside of and above the porous TiO_2.

3. Enlargement of cell

Enlargement of the cell area is especially mandatory to enable the use of perovskite devices such as actual commercial solar cell panels [38]. The photovoltaic properties of perovskite-type solar cells with a substrate size of 70 mm × 70 mm were investigated [39].

The photovoltaic devices consisted of a $CH_3NH_3PbI_3$ compound layer, TiO_2 electron transport layers, and spiro-OMeTAD hole-transport layer, prepared by a simple spin-coating technique. The effect of the distance from the center of the cell on conversion efficiency was investigated based on light-induced J–V curves and IPCE measurements. A photograph of a perovskite solar cell measuring 70 mm × 70 mm and a schematic illustration of the arrangement of Au electrodes on the substrate are shown in **Figure 9(a)** and **(b)**, respectively.

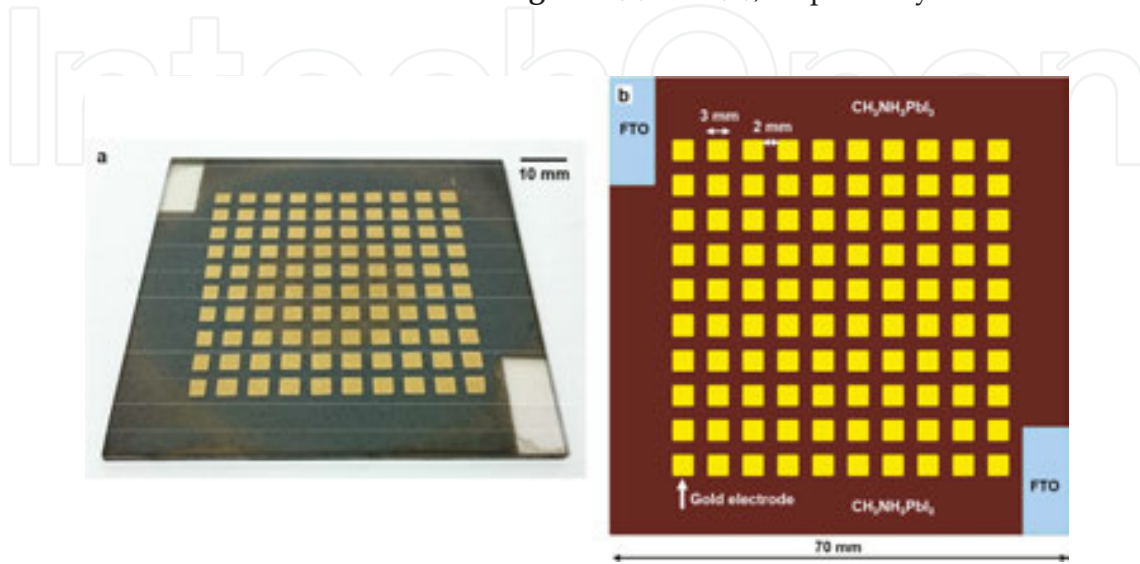**Figure 9.** (a) Photograph of perovskite solar cell measuring 70 mm × 70 mm. (b) Schematic illustration of arrangement of Au electrodes on the substrate.

The measured short-circuit current density, open-circuit voltage, fill factor, and photoconversion efficiency of the present $TiO_2/CH_3NH_3PbI_3$ cell as a function of the distance from the center of the cell are shown in **Figure 10(a–d)**, respectively. The highest efficiency was obtained for the electrode at 12.7 mm from the cell center, which provided a photoconversion efficiency of 3.15%, a V_{OC} of 0.653 V, a J_{SC} of 13.0 mA cm^{-2}, and a FF of 0.371. Due to the long diffusion length of exciton [40], the J_{SC} values were nearly constant at ~12 mA cm^{-2} for all electrodes on the solar cell, as observed in **Figure 10(a)**. Although the FF value slightly decreased as the distance (d) from the center of the cell increased, the deviation was small, as observed in **Figure 9(c)**. On the other hand, the value of V_{OC} depended fairly on the d values, as observed in **Figure 10(b)**, which led to decreased efficiency, as shown in **Figure 10(d)**. The dependency of V_{OC} values on the d values might be related to the thickness of $CH_3NH_3PbI_3$ layer prepared on the large substrate by the spin-coating method. The low V_{OC} and FF values would be related to the coverage ratio of $CH_3NH_3PbI_3$ at the $TiO_2/CH_3NH_3PbI_3$ interface, and further multiple spin-coating of $CH_3NH_3PbI_3$ layers on the TiO_2 mesoporous layer would improve the coverage of $CH_3NH_3PbI_3$ on the TiO_2 mesoporous layer, which would induce the increase in the conversion efficiency of the solar cells.

IPCE spectra of electrodes at 4.2, 12.7, and 22.8 mm from the cell center are shown in **Figure 10(e)**. All spectra show similar changes on the wavelength, which agrees with the J_{SC} results shown in **Figure 9(a)**. The perovskite $CH_3NH_3PbI_3$ structure showed photoconversion within the whole measurement range of 300–800 nm, which nearly agrees with the

reported energy gaps for the $CH_3NH_3PbI_3$ phase. Control of the energy levels of the conduction band and valence band is important for carrier transport in the cell. The conversion efficiencies obtained for the present cells are lower than the previously reported values. It might be difficult to control the uniformity of the layer thickness and interfacial structure using the spin-coating. In the present work, the samples were prepared in air, which might result in a decrease in the efficiency of the present cells, and perovskite crystals with higher quality and a uniform surface should be prepared in future works.
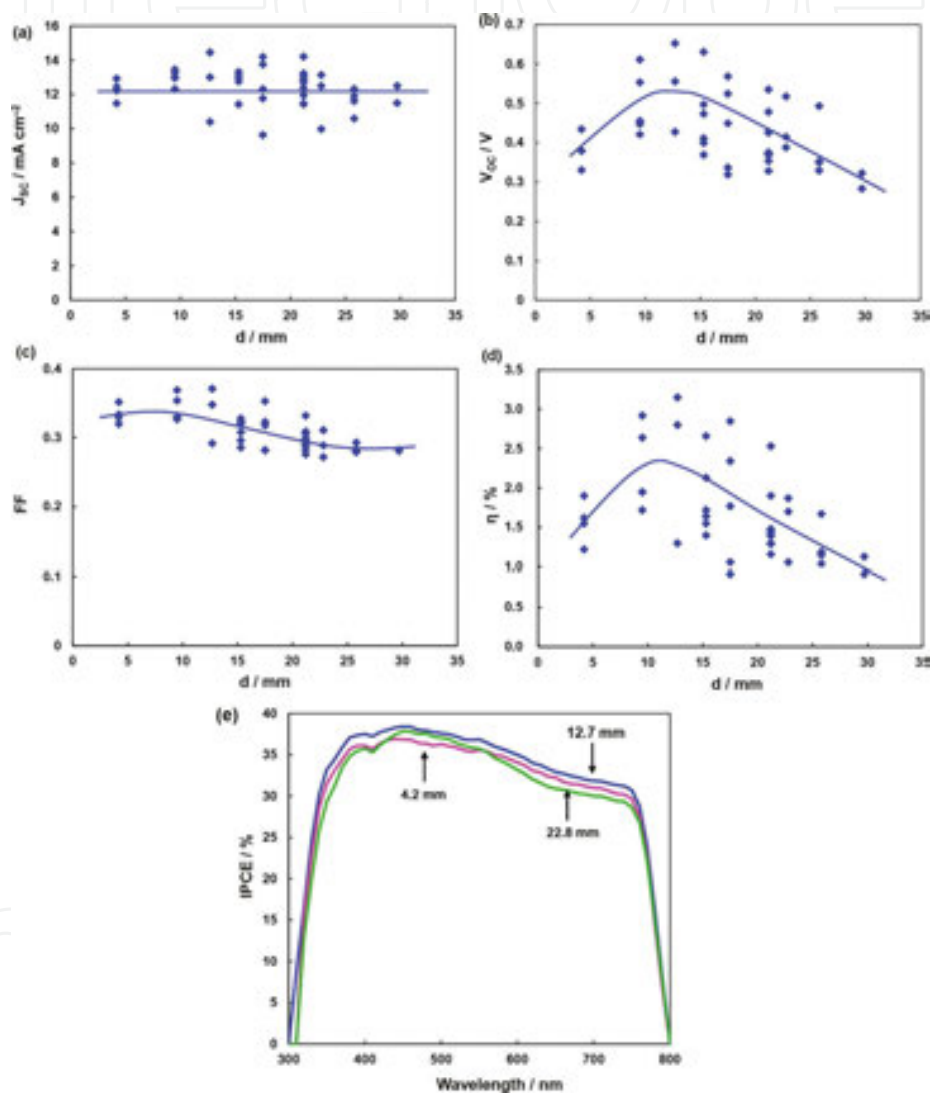

Figure 10. Measured (a) short-circuit current density; (b) open-circuit voltage; (c) fill factor and (d) conversion efficiency of TiO_2/$CH_3NH_3PbI_3$ cell as a function of the distance from the center of the cell. (e) IPCE spectra of the same cell.

As a summary, perovskite solar cell devices with a substrate size of 70 mm were produced by a spin-coating method using a mixture solution. The photovoltaic properties of the solar cells and the size effect of the substrate were investigated by *J–V* and IPCE measurements, and the dependency of their conversion efficiency on the distance from the center of the cell was

investigated. Nearly constant values of short-circuit current density were obtained over a large area, due to the long exciton diffusion length of the $CH_3NH_3PbI_3$ compound. The open-circuit voltage fairly depended on the distance from the center of the cell, which led to a change in conversion efficiency. Optimizing the layer thickness and structure would be important for improving the performance of the devices.

4. Electron transport layers

The electron-transport layers (ETLs) such as TiO_2 are also important for the $CH_3NH_3PbI_3$-based photovoltaic devices. Here, niobium (V) ethoxide was chosen as an additional chemical for TiO_2 [41]. When niobium (Nb) atoms with five valence electrons are introduced at Ti sites with four valence electrons, extra electrons are introduced in the 3d band and could work as a donor. Since the energy level of impurity in the TiO_2 band gap is shallow, transparency could be conserved after the Nb doping [42–46]. Additionally, the radius of Nb ion is close to that of the Ti ion, which leads to a solid solution of titanium and niobium in the anatase-type TiO_2 crystal. The TiO_2 crystal added with Nb is denoted as $Ti(Nb)O_2$ here.

The XRD patterns and crystal structure of TiO_2 and $Ti(Nb)O_2$ thin films on the FTO substrate are shown in **Figure 11(a)** and **(b)**, respectively. Diffraction peaks of TiO_2 101 are observed, and the intensity increased upon Nb-doping. The XRD data indicate that the d-spacing of $Ti(Nb)O_2$ (1.802 Å) is almost the same as that of TiO_2 (1.807 Å). The crystallite size seems to increase a little upon Nb addition (28 nm) to TiO_2 (24 nm).
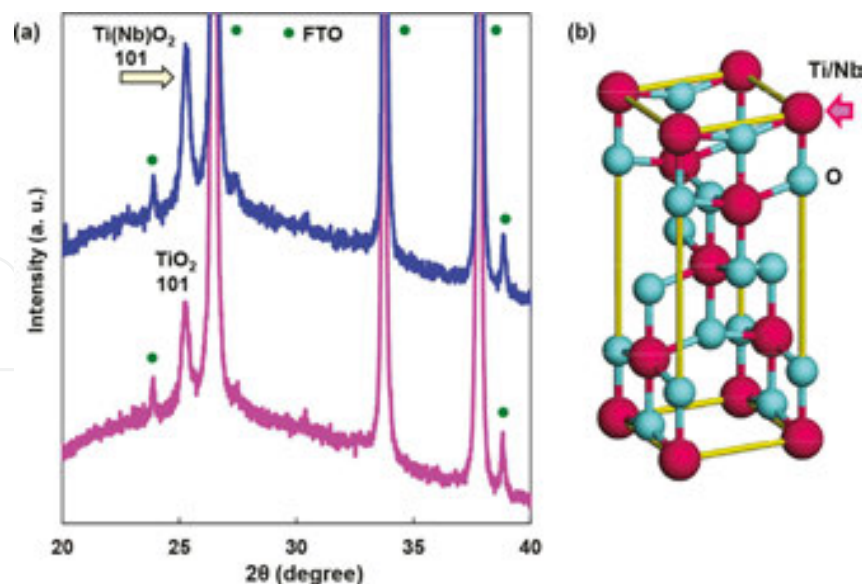

Figure 11. (a) XRD patterns of TiO_2 and $Ti(Nb)O_2$ thin films on FTO. (b) Crystal structure of TiO_2.

A scanning electron microscopy (SEM) image of the $Ti(Nb)O_2$ thin film is shown in **Figure 12(a)**, and the image indicates several particles with sizes of ca. 1 µm on the

smooth surface. Elemental mapping images of Ti and Nb using SEM with energy-dispersive X-ray spectroscopy (EDX) are shown in **Figure 12(b)** and **(c)**, respectively, which indicate that Ti and Nb elements are homogeneously distributed in the films. The elemental ratio of Ti:Nb was estimated to be ~1.00:0.10 from SEM-EDX analysis. The dispersed particles observed in **Figure 12(a)** were found to be Nb-rich phase, as observed in **Figure 12(c)**, which resulted in an Nb-rich (ca. 9 atomic %) composition compared with the preparation composition (ca. 5 atomic %). From XRD analysis, no diffraction peak corresponding to Nb and Nb_2O_5 was observed.
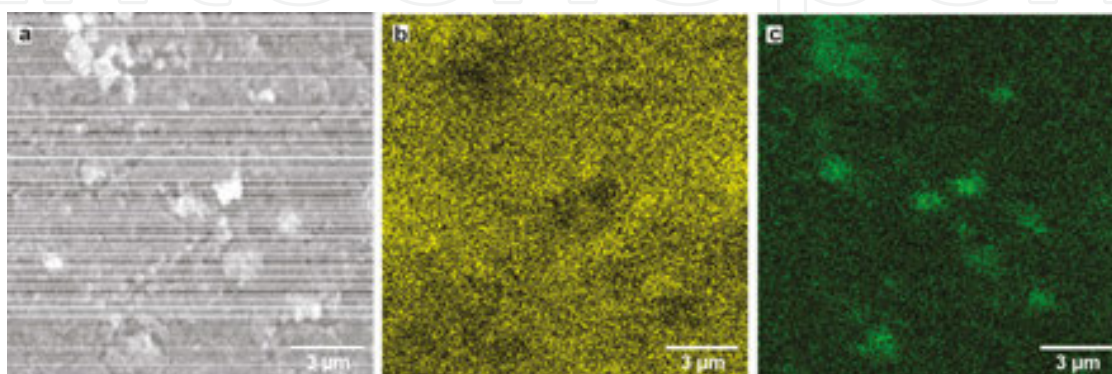

Figure 12. (a) SEM image of Ti(Nb)O_2 thin film. Elemental mapping of (b) Ti (Lα) and (c) Nb (Lα).

The sheet resistances of TiO_2 and Ti(Nb)O_2 thin films were measured to be 1.7×10^6 and 4.2×10^4 Ω/sq, respectively. The sheet resistance significantly decreased upon Nb addition. The J–V characteristics of Ti(Nb)O_2/$CH_3NH_3PbI_3$/spiro-OMeTAD photovoltaic cells under illumination are shown in **Figure 13(a)**. The detailed parameters of the best device are listed in **Table 2**. The Ti(Nb)O_2/$CH_3NH_3PbI_3$ photovoltaic cell provided an η of 6.63%, a FF of 0.416, a J_{SC} of 20.8 mA cm^{-2}, and a V_{OC} of 0.768 V. The J_{SC} value was especially improved upon Nb
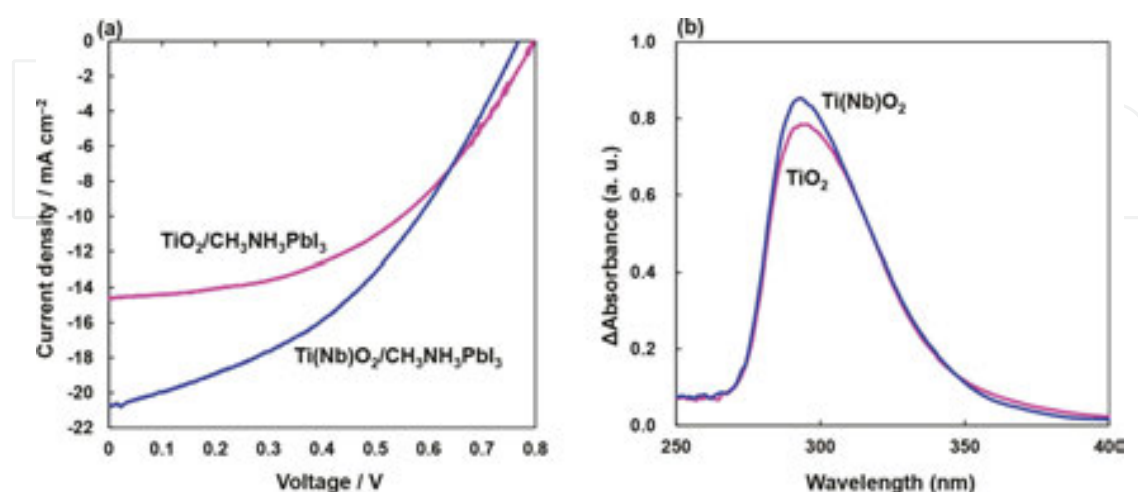

Figure 13. (a) J–V characteristics of Ti(Nb)O_2/$CH_3NH_3PbI_3$ photovoltaic cells. (b) Differential absorption spectra of TiO_2 and Ti(Nb)O thin films.

addition, which resulted in increased conversion efficiency. The averaged efficiency (η_{ave}) of three electrodes on the cells is 6.46%, as listed in **Table 2**.

ETL	J_{SC} (mA cm^{-2})	V_{OC} (V)	FF	η (%)	η_{ave} (%)
TiO$_2$	14.6	0.796	0.478	5.56	5.03
Ti(Nb)O$_2$	20.8	0.768	0.416	6.63	6.46

Table 2. Measured parameters of Ti(Nb)O$_2$/CH$_3$NH$_3$PbI$_3$ cells.

Figure 13(b) shows differential absorption spectra of FTO/TiO$_2$ and FTO/Ti(Nb)O$_2$ after subtracting the spectrum of the FTO substrate. These absorption spectra appear to be closely equal. Based on the band structure of indirect transition [60], energy gaps for TiO$_2$ and Ti(Nb)O$_2$ were estimated to be 3.54 and 3.52 eV from **Figure 13(b)**, respectively, which indicate that the energy gaps are almost the same for TiO$_2$ and Ti(Nb)O$_2$.
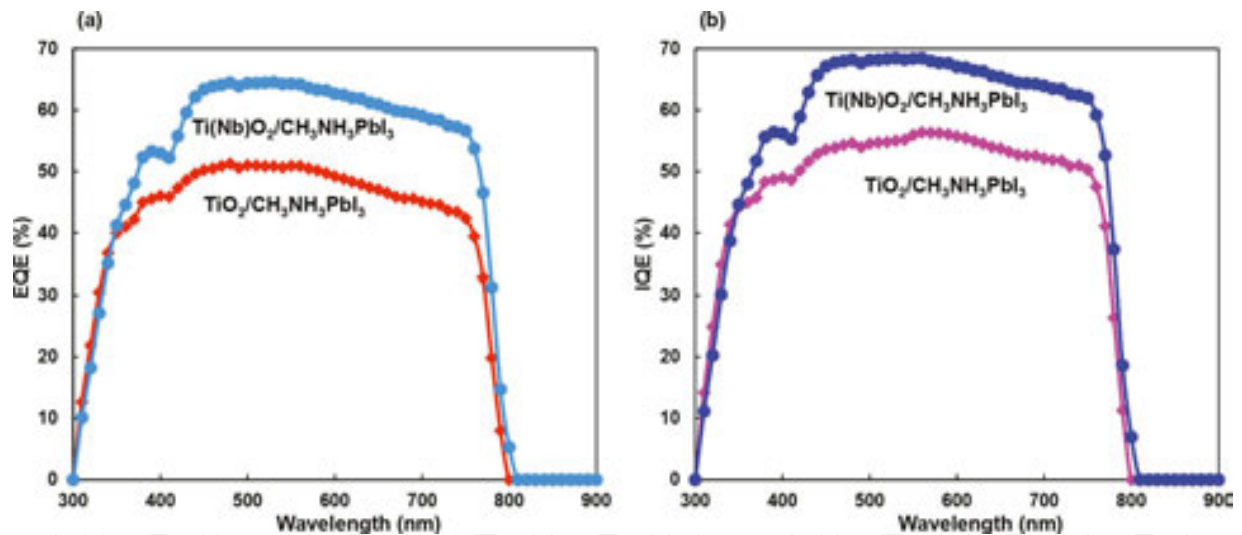

Figure 14. (a) EQE and (b) IQE spectra of Ti(Nb)O$_2$/CH$_3$NH$_3$PbI$_3$ cells.

The IPCE of the cells was also investigated, and the external quantum efficiency (EQE) and internal quantum efficiency (IQE) were measured by a spectral response system. The EQE spectra of the photovoltaic cells with the Ti(Nb)O$_2$/CH$_3$NH$_3$PbI$_3$/spiro-OMeTAD structure are shown in **Figure 14(a)**. The perovskite CH$_3$NH$_3$PbI$_3$ phase shows photoconversion efficiencies between 300 and 800 nm. By Nb addition into the TiO$_2$ layer, the perovskite CH$_3$NH$_3$PbI$_3$ structure shows high EQE values of ca. 60% at 500–600 nm and ca. 5% at 800 nm, and the EQE was 0% for ordinary TiO$_2$ at 800 nm. The IQE spectra of Ti(Nb)O$_2$/CH$_3$NH$_3$PbI$_3$/spiro-OMeTAD cells were computed from the reflectance and EQE, as shown

in **Figure 14(b)**. The IQE of both cells increased in the range of 500–800 nm, which implies that suppression of reflection of light in the range of 500–800 nm could increase the photo-conversion efficiencies of the cells. High IQE values of ~70% are seen in the range of 500–600 nm by the Nb addition in the TiO_2 layer.

Two mechanisms could be considered for the decrease in the sheet resistances of TiO_2 by the Nb addition. The first mechanism is niobium doping at the titanium sites in the TiO_2 crystal. Owing to the XRD and differential absorption results of **Figures 11(a)** and **13(b)**, the TiO_2 phase still preserved the crystal structure, energy gap, and transparency of ana-tase TiO_2. In addition, a small amount of Nb atoms are widely distributed in the TiO_2 phase, as observed by SEM-EDX of **Figure 10(c)** and **(d)**, which could imply a solid solu-tion of titanium and niobium in the TiO_2 structure. The extra electron of Nb might be intro-duced into the 3d band of Ti and behaves as a donor [60]. The second conceivable mechanism is enhancement of carrier transport by formation of niobium-based particles in the TiO_2 layer, as observed in SEM-EDX images. Nanoparticles in electron-transport and hole-transport layers could facilitate the carrier transport [47, 48], and the present niobium-based particles might contribute to the carrier transport. Both mechanisms could provide an increase in carrier concentration and transport, and an improvement of conversion effi-ciency through the increase in J_{SC}.

As a summary, $Ti(Nb)O_2/CH_3NH_3PbI_3$-based photovoltaic devices were fabricated by a spin-coating method using a mixture solution of niobium(V) ethoxide, and the effects of Nb addition into the TiO_2 layer were investigated. By adding a simple solution of niobi-um(V) ethoxide to the TiO_2 precursor solutions, the sheet resistance of the $Ti(Nb)O_2$ thin film decreased, and the J_{SC} value increased, which resulted in the increase in conversion efficiency.

5. Halogen doping to $CH_3NH_3PbI_3$

Effects of Cl-doping $CH_3NH_3PbI_3$ using a mixture solution of perovskite compounds on the microstructures and photovoltaic properties have been investigated [49]. The *J–V* char-acteristics of the $TiO_2/CH_3NH_3PbI_{3-x}Cl_x$/spiro-OMeTAD photovoltaic cells under illumina-tion are shown in **Figure 15(a)**, which indicate an effect of Cl-doping to the $CH_3NH_3PbI_3$ layer. Measured photovoltaic parameters of $TiO_2/CH_3NH_3PbI_{3-x}Cl_x$ cells are summarized in **Table 3**. The $CH_3NH_3PbI_3$ cell provided a power conversion efficiency of 6.16%, and the averaged efficiency of four electrodes on the cells is 5.53%, as listed in **Table 3**. The highest efficiency was obtained for the $CH_3NH_3PbI_{2.88}Cl_{0.12}$ cell, which provided an *η* of 8.16%, a *FF* of 0.504, J_{SC} of 18.6 mA cm^{-2}, and a V_{OC} of 0.869 V. As a Cl composition increased, the J_{SC} and V_{OC} decreased, as shown in **Figure 15(b)** and **Table 3**. Energy gaps (E_g) of $CH_3NH_3PbI_3$, $CH_3NH_3PbI_{2.88}Cl_{0.12}$, and $CH_3NH_3PbI_{1.8}Cl_{1.2}$ were estimated to be 1.578, 1.590, and 1.593, respectively, from the optical absorption, which indicated the energy gap of $CH_3NH_3PbI_3$ increased by the Cl-doping.

Preparation composition	J_{SC} (mA cm^{-2})	V_{OC} (V)	FF	η (%)	η_{ave} (%)
$CH_3NH_3PbI_3$	17.5	0.844	0.416	6.16	5.53
$CH_3NH_3PbI_{2.94}Cl_{0.06}$	17.7	0.871	0.487	7.53	6.02
$CH_3NH_3PbI_{2.92}Cl_{0.08}$	18.1	0.825	0.478	7.14	6.52
$CH_3NH_3PbI_{2.88}Cl_{0.12}$	18.6	0.869	0.504	8.16	7.77
$CH_3NH_3PbI_{2.77}Cl_{0.23}$	13.9	0.865	0.440	5.29	4.97
$CH_3NH_3PbI_{2.65}Cl_{0.35}$	11.7	0.709	0.347	2.87	2.51
$CH_3NH_3PbI_{1.80}Cl_{1.20}$	14.8	0.598	0.436	3.87	2.00

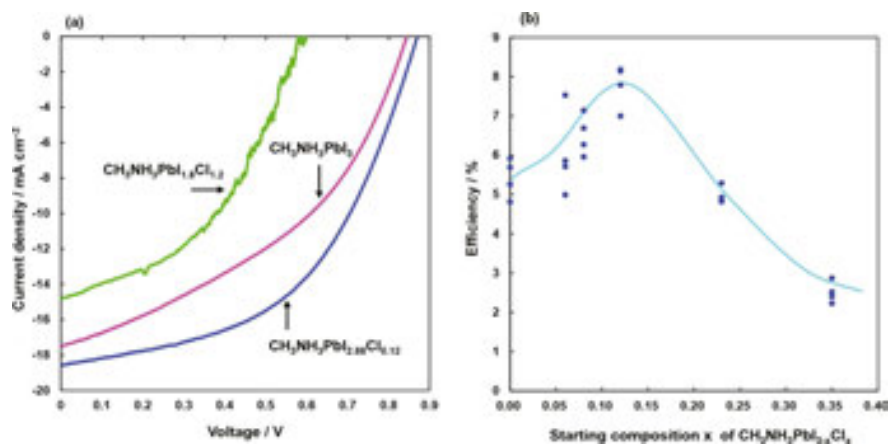**Table 3.** Measured photovoltaic parameters of $TiO_2/CH_3NH_3PbI_{3-x}Cl_x$ cells.

Figure 15. (a) J–V characteristic of $TiO_2/CH_3NH_3PbI_{3-x}Cl_x$ photovoltaic cells. (b) Conversion efficiencies of the cells as a function of Cl concentration.
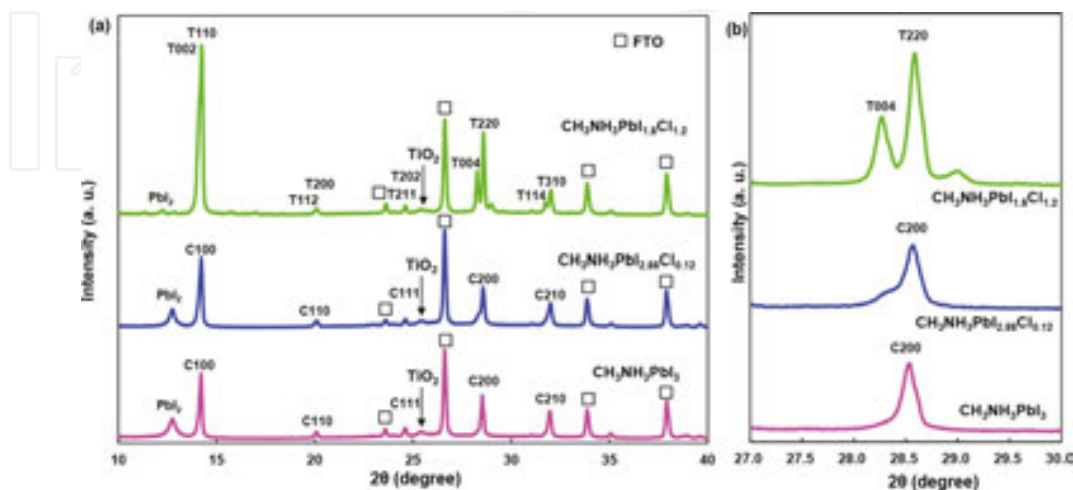

Figure 16. (a) XRD patterns of $CH_3NH_3PbI_{3-x}Cl_x$ thin films. (b) Enlarged XRD patterns at 2θ of ~28.5°.

Preparation composition	Crystal system	Lattice constant (Å)	V (Å³)	Z	V/Z (Å³)
$CH_3NH_3PbI_3$	Cubic	$a = 6.2524$	244.42	1	244.42
$CH_3NH_3PbI_{2.88}Cl_{0.12}$	Pseudocubic	$a = 6.2446$	243.51	1	243.51
$CH_3NH_3PbI_{1.80}Cl_{1.20}$	Tetragonal	$a = 8.8255$	982.81	4	245.70
		$c = 12.6180$			

V: unit cell volume; Z: number of chemical units in the unit cell.

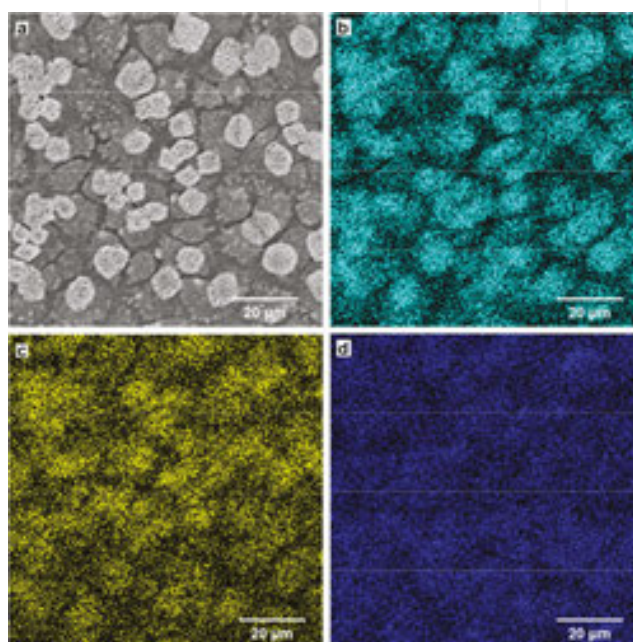**Table 4.** Measured and reported structural parameters of $CH_3NH_3PbI_{3-x}Cl_x$.

Figure 17. (a) SEM image of $TiO_2/CH_3NH_3PbI_{2.88}Cl_{0.12}$. Elemental mapping images of (b) Pb Mα line, (c) I Lα line, and (d) Cl Kα line.

XRD patterns of $CH_3NH_3PbI_{3-x}Cl_x$ thin films on the FTO/TiO$_2$ are shown in **Figure 16(a)**. The temperature for XRD measurements was ~292 K. The diffraction peaks can be indexed by cubic and tetragonal crystal systems for $CH_3NH_3PbI_3$ and $CH_3NH_3PbI_{1.8}Cl_{1.2}$ films, respectively. Although the deposited films are a single perovskite phase, broader diffraction peaks due to PbI$_2$ compound appeared in the $CH_3NH_3PbI_3$ film, as shown in **Figure 16(a)**. **Figure 16(b)** shows enlarged XRD patterns at 2θ of ~28.5°. A diffraction peak of 200 for the $CH_3NH_3PbI_3$ split into diffraction peaks of 004/220 for the $CH_3NH_3PbI_{1.8}Cl_{1.2}$ by the heavy Cl-doping, which indicates the structural transformation from the cubic to tetragonal crystal systems [19]. The heavy Cl-doping suppressed the formation of PbI$_2$, and no PbCl$_2$ was detected for the $CH_3NH_3PbI_{1.8}Cl_{1.2}$. For the $CH_3NH_3PbI_{2.88}Cl_{0.12}$, a small shoulder is observed just left of the 200 reflection as shown in **Figure 16(b)**, which would be due to the pseudocubic structure between the cubic and tetragonal phases. The measured structural parameters of the $CH_3NH_3PbI_{3-x}Cl_x$ are summarized in **Table 4**.

Figure 17(a) is a SEM image of $TiO_2/CH_3NH_3PbI_{2.88}Cl_{0.12}$, and the image shows particles with sizes of ca. 10 μm. Mapping images of Pb, I, and Cl elements by SEM equipped with EDX are shown in **Figure 17(b–d)**, respectively. These mapping images of elements indicate that the dispersed particles observed in **Figure 17(a)** correspond to the perovskite $CH_3NH_3PbI_{3-x}Cl_x$ phase. The composition ratio of Pb:I:Cl was 1.00:2.70:0.11, which was calculated from their EDX spectra using each element's line after background correction by normalizing the spectrum peaks on the atomic concentration of Pb element. The present result indicates that iodine atoms would be deficient comparing with the starting composition of $CH_3NH_3PbI_{2.88}Cl_{0.12}$, and the deficient I might increase the hole concentration. The $CH_3NH_3PbI_3$ crystals have perovskite structures, and provide structural transitions from tetragonal to cubic system upon heating at ~330 K [27–29].

The XRD results in **Figure 16** indicated phase transformation of the $CH_3NH_3PbI_3$ perovskite structure from tetragonal to cubic system by partial separation of PbI_2 from $CH_3NH_3PbI_3$ phase through the annealing [35], which is related to decrease in the unit cell volume of the cubic $CH_3NH_3PbI_3$ phase from the normal 261 $Å^3$ to the present 244 $Å^3$, as shown in **Table 4**. From the SEM-EDX results, the site occupancies of I atom might be smaller than 1, which would also decrease the cell volume. The conversion efficiencies were reported to be increased by the tetragonal to cubic transformation [35].

The X-ray diffraction pattern indicates division of diffraction peaks from C200 to T004/T220 by means of heavy Cl-doping. This designates reduction of the symmetry of the crystal structures from the cubic to tetragonal system, which resulted in decrease of the photoconversion efficiencies. Once a small amount of Cl was added in the $CH_3NH_3PbI_3$ phase, the cubic structure was still preserved as the pseudocubic phase. The doped Cl atoms would lengthen diffusion length of excitons [7, 40], which would result in the increase of the efficiencies.

EQE spectra of the photovoltaic cell with the $TiO_2/CH_3NH_3PbI_3$-xClx/spiro-OMeTAD structure are shown in **Figure 18(a)**. The perovskite $CH_3NH_3PbI_3$ phase shows photoconversion efficiencies between 300 and 800 nm. In the present work, the energy gap of the $CH_3NH_3PbI_3$ phase increased from 1.578 to 1.590 eV by Cl-doping, which could contribute to the increase in open-circuit voltage. IQE spectra of $TiO_2/CH_3NH_3PbI_3$ and $TiO_2/CH_3NH_3PbI_{2.92}Cl_{0.08}$ were computed from EQE spectra and reflectance, as shown in **Figure 18(b)**. The IQE of both cells increased in the wavelength range of 500–800 nm, and this indicates that improvement of the optical absorption in that range might improve the photoconversion efficiencies of $TiO_2/CH_3NH_3PbI_{3-x}Cl_x$/spiro-OMeTAD cells.

In summary, $TiO_2/CH_3NH_3PbI_{3-x}Cl_x$-based photovoltaic devices were fabricated by a spin-coating method using a mixture solution, and effects of $PbCl_2$ addition to the perovskite $CH_3NH_3PbI_3$ precursor solutions on the photovoltaic properties were investigated. The microstructure analysis showed phase transformation of the perovskite structure from cubic to tetragonal system by heavy Cl-doping to the $CH_3NH_3PbI_3$ phase. A small amount of Cl-doping ($CH_3NH_3PbI_{2.9}Cl_{0.1}$) at iodine sites increased the efficiencies up to ~8%, and it might be owing to conservation of the cubic perovskite structure and to extension of diffusion length of excitons and energy gap. Both the EQE and IQE increased in the range of 300–800 nm by means of a small amount of Cl-doping, and the IQE data designate that the inhibition of the optical

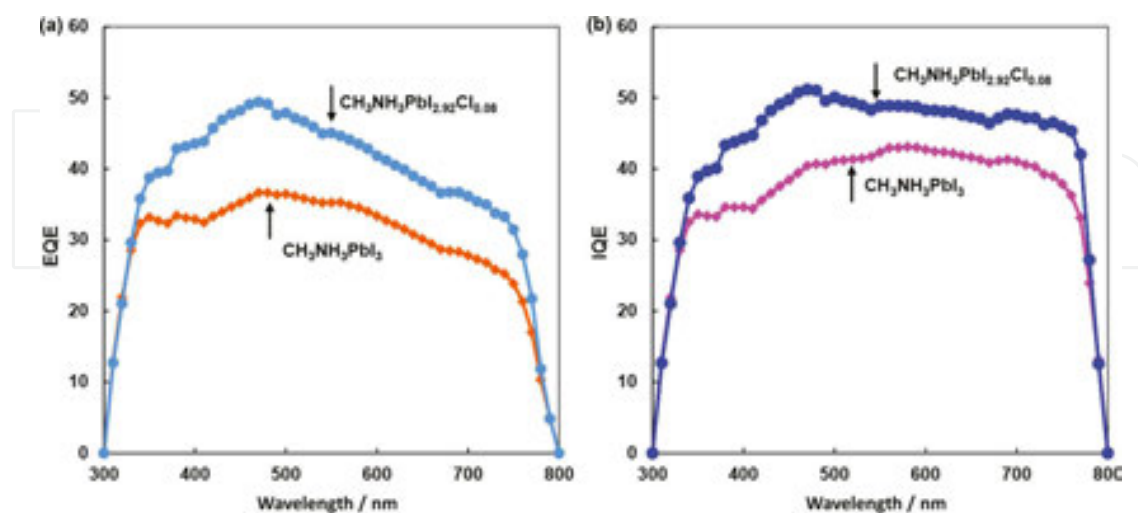reflection in the wavelength range of 500–800 nm might improve the photoconversion efficiencies further.

Figure 18. (a) EQE and (b) IQE spectra of $CH_3NH_3PbI_3$ and $CH_3NH_3PbI_{2.92}Cl_{0.08}$ cells.

6. Metal doping to $CH_3NH_3PbI_3$

The properties of solar cells are dependent on the atomic compositions and the crystal structures of perovskite $CH_3NH_3PbI_3$ compounds. Metal atom and halogen doping such as tin (Sn) and chlorine (Cl)/bromine (Br) at the Pb and I sites, respectively, in the $CH_3NH_3PbI_3$ structure have been investigated [12–14, 50–52]. Particularly, researches of the metal element doping at Pb sites are fascinating in the view of Pb-free devices and influence on the photovoltaic properties.

The objective here is to investigate photovoltaic properties and microstructures of photovoltaic devices with perovskite-type $CH_3NH_3Pb_{1-x}Sb_xI_3$ compounds, prepared by a spin-coating technique in ordinary air. Antimony (Sb) is an element in the group 15 and might work as electronic carriers at the Pb sites in the group 14. Effects of SbI_3 addition to a $CH_3NH_3PbI_3$ mixed solution on the microstructures and photovoltaic properties were investigated [53, 54].

The $J–V$ characteristics of the $TiO_2/CH_3NH_3Pb_{1-x}Sb_xI_3$/spiro-OMeTAD photovoltaic cells under illumination are shown in **Figure 19(a)**, which indicate an effect of Sb addition to $CH_3NH_3PbI_3$. The measured photovoltaic parameters of $TiO_2/CH_3NH_3Pb_{1-x}Sb_xI_3$ cells are summarized in **Table 5**.

The $CH_3NH_3PbI_3$ cell provided a power conversion efficiency of 6.56%, and the averaged efficiency of four electrodes on the cells is 6.37%, as listed in **Table 5**. The highest efficiency was obtained for the $CH_3NH_3Pb_{0.97}Sb_{0.03}I_3$ cell, which provided an η of 9.07%, a FF of 0.560, a J_{SC} of 19.2 mA cm^{-2}, and a V_{OC} of 0.843V. As the x value (preparation composition of Sb)

increased, the efficiencies decreased, as shown in **Figure 19(b)** and **Table 5**. An η of 9.7% was also reported by addition of SbI_3 and NH_4Cl to the $CH_3NH_3PbI_3$ [54].

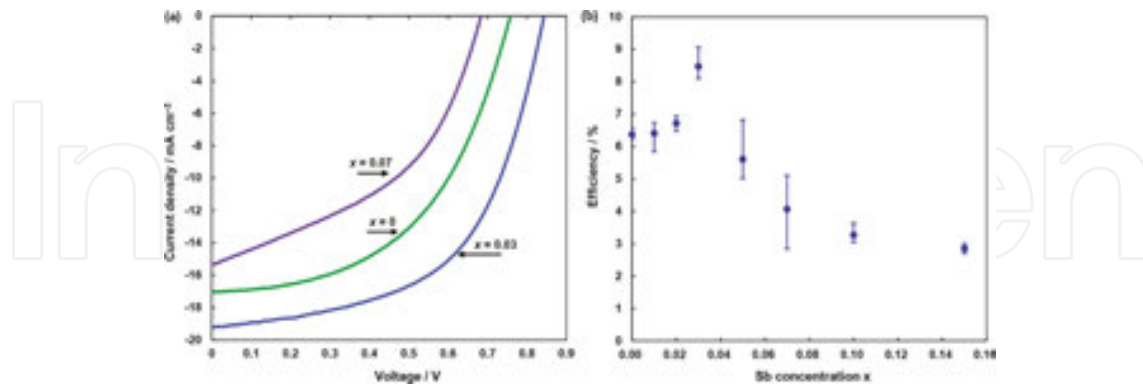**Figure 19.** (a) J–V characteristics of $TiO_2/CH_3NH_3Pb_{1-x}Sb_xI_3$ photovoltaic cells. (b) Conversion efficiencies of $CH_3NH_3Pb_{1-x}Sb_xI_3$ as a function of Sb concentration.

Sb (x)	J_{SC} (mA cm^{-2})	V_{OC} (V)	FF	η (%)	η_{ave} (%)
0.00	17.0	0.758	0.509	6.56	6.37
0.01	16.0	0.789	0.534	6.74	6.41
0.02	16.9	0.792	0.518	6.94	6.72
0.03	19.2	0.843	0.560	9.07	8.47
0.05	15.7	0.755	0.575	6.82	5.61
0.07	14.7	0.692	0.502	5.11	4.07
0.10	12.1	0.630	0.476	3.63	3.27
0.15	13.1	0.570	0.402	3.00	2.85

Preparation compositions of Sb are indicated by x.

Table 5. Measured photovoltaic parameters of $TiO_2/CH_3NH_3Pb_{1-x}Sb_xI_3$ cells.

IPCE spectra of the $CH_3NH_3PbI_3$ and $CH_3NH_3Pb_{0.97}Sb_{0.03}I_3$ cells are shown in **Figure 20**. The perovskite $CH_3NH_3Pb_{1-x}Sb_xI_3$ shows photoconversion efficiencies between 300 and 800 nm. The IPCE was improved in the range of 350–770 nm by adding a small amount of Sb.

XRD patterns of $CH_3NH_3Pb_{1-x}Sb_xI_3$ cells on the FTO/TiO_2 are shown in **Figure 21(a)**. The diffraction peaks can be indexed by a cubic crystal system (Pm3m) for the $CH_3NH_3Pb_{1-x}Sb_xI_3$ thin films. Although the deposited films are a single perovskite structure, broader diffraction peaks due to the PbI_2 compound appeared in the $CH_3NH_3PbI_3$ film, as shown in **Figure 21(a)**. The Sb addition suppressed the formation of PbI_2, and most of PbI_2 was not detected for the $CH_3NH_3Pb_{1-x}Sb_xI_3$ cells with $x > 0.03$. **Figure 21(b)** shows measured lattice constants a of $CH_3NH_3Pb_{1-x}Sb_xI_3$ as a function of Sb concentration. A small

increase in lattice constants a is observed for $x = 0.03$ and 0.05, and further addition of Sb decreases the lattice constants, which seems to be a significant difference from the error bar. The XRD result of $CH_3NH_3PbI_3$ in **Figure 21(a)** showed the existence of PbI_2 after annealing at 100°C for 15 min. This would indicate partial separation of PbI_2 from $CH_3NH_3PbI_3$ after annealing, which also might correspond to the smaller lattice constant a (6.266 Å) of the cubic perovskite structure, compared with that (6.391 Å) of $CH_3NH_3PbI_3$ single crystal reported in Ref. [27].

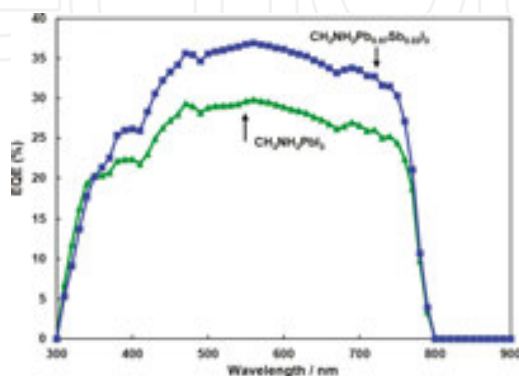**Figure 20.** IPCE spectra of $CH_3NH_3PbI_3$ and $CH_3NH_3Pb_{0.97}Sb_{0.03}I_3$ cells.
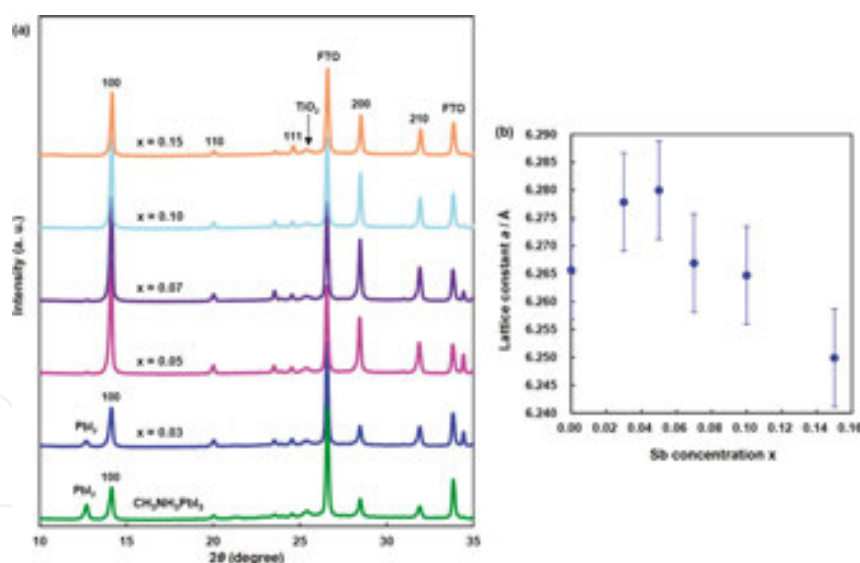
Figure 21. (a) XRD patterns of $CH_3NH_3Pb_{1-x}Sb_xI_3$ solar cells. (b) Lattice constants a of $CH_3NH_3Pb_{1-x}Sb_xI_3$ as a function of Sb concentration.

Increase in the photoconversion efficiencies could be explained by two mechanisms. The first mechanism is Sb doping effect at the Pb atom sites. The ionic valence of Sb is three, and it is higher compared with that of Pb^{2+}. Then, the excess charge of Sb^{3+} might work as carriers in the $CH_3NH_3Pb_{1-x}Sb_xI_3$ crystal, and the J_{SC} values were improved. The second mechanism is described as follows: I^- ions might be attracted at the I sites by Sb^{3+} with more ionic valence

compared with that of Pb^{2+}, which resulted in the suppression of PbI_2 elimination from $CH_3NH_3PbI_3$ and in the increase of lattice constants a of $CH_3NH_3PbI_3$. The suppression of PbI_2 would improve the interfacial structure of $TiO_2/CH_3NH_3PbI_3$, which might result in improvement of V_{OC}. The lattice constants are expected to be decreased by an increase in the amount of Sb with an ionic size smaller than Pb. Other elemental dopings such as Ge, Tl, and In at the Pb sites were also reported [55, 56].

In summary, $TiO_2/CH_3NH_3Pb_{1-x}Sb_xI_3$-based photovoltaic devices were fabricated, and the effects of SbI_3 addition to the perovskite $CH_3NH_3PbI_3$ precursor solutions on the photovoltaic properties were investigated. The microstructures of the devices indicated that the lattice constant of $CH_3NH_3Pb_{1-x}Sb_xI_3$ increased a little, and that the formation of PbI_2 was inhibited by the addition of a small amount of Sb, which led to the improvement of the conversion efficiencies to ~9%. The IPCE also increased in the range of 350–770 nm by the addition of Sb.

7. Conclusion

Various $TiO_2/CH_3NH_3PbI_3$-based photovoltaic devices were fabricated and characterized. Especially, effects of metal doping and halogen doping to the perovskite and TiO_2 were investigated. Microstructure analysis indicated the changes of the perovskite structure, which resulted in the improvement of photovoltaic properties of the devices. Various elemental dopings to the perovskite structure could be studied further both by experiments and theoretical calculations as follows: Cs, Rb, and K doping to the CH_3NH_3 positions for stability of the structure; Ge, Sn, and Sb doping to the Pb positions for improvement of the semiconducting properties; Cl, Br, and F doping to the I positions for enhancement of carrier mobility.

Acknowledgements

Author details

Takeo Oku[*], Masahito Zushi, Kohei Suzuki, Yuya Ohishi, Taisuke Matsumoto and Atsushi Suzuki

*Address all correspondence to: oku@mat.usp.ac.jp

Department of Materials Science, The University of Shiga Prefecture, Hikone, Shiga, Japan

References

[1]   Kojima A, Teshima K, Shirai Y, Miyasaka T (2009). Organometal halide perovskites as visible-light sensitizers for photovoltaic cells. Journal of the American Chemical Society, 131, 6050–6051.

[2]   Im J-H, Lee C-R, Lee J-W, Park S-W, Park N-G (2011). 6.5% efficient perovskite quantum-dot-sensitized solar cell. Nanoscale, 3, 4088–4093.

[3]   Kim HS, Lee CR, Im JH, Lee KB, Moehl T, Marchioro A, Moon SJ, Yum JH, Humphry-Baker R, Moser JE, et al (2012). Lead iodide perovskite sensitized all-solid-state submicron thin film mesoscopic solar cell with efficiency exceeding 9%. Scientific Reports, 2, 591–1–591–7.

[4]   Grinberg I, West DV, Torres M, Gou G, Stein DM, Wu L, Chen G, Gallo EM, Akbashev A, Davies PK, et al. Perovskite oxides for visible-light-absorbing ferroelectric and photovoltaic materials. Nature, 2013, 503, 509–512.

[5]   Lee MM, Teuscher J, Miyasaka T, Murakami TN, Snaith HJ (2012). Efficient hybrid solar cells based on meso-superstructured organometal halide perovskites. Science, 338, 643–647.

[6]   Chung I, Lee B, He JQ, Chang RPH, Kanatzidis MG (2012). All-solid-state dye-sensitized solar cells with high efficiency. Nature, 485, 486–489.

[7]   Stranks SD, Eperon GE, Grancini G, Menelaou C, Alcocer MJP, Leijtens T, Herz LM, Petrozza A, Snaith HJ (2013). Electron-hole diffusion lengths exceeding 1 micrometer in an organometal trihalide perovskite absorber. Science, 342, 341–344.

[8]   Burschka J, Pellet N, Moon S-J, Humphry-Baker R, Gao P, Nazeeruddin MK, Grätzel M (2013). Sequential deposition as a route to high-performance perovskite-sensitized solar cells. Nature, 499, 316–320.

[9]   Liu M, Johnston MB, Snaith HJ. Efficient planar heterojunction perovskite solar cells by vapour deposition (2013). Nature, 501, 395–398.

[10] Liu D, Kelly TL (2014). Perovskite solar cells with a planar heterojunction structure prepared using room-temperature solution processing techniques. Nature Photonics, 8, 133–138.

[11] Wang JT-W, Ball JM, Barea EM, Abate A, Alexander-Webber JA, Huang J, Saliba M, Mora-Sero I, Bisquert J, Snaith HJ, Nicholas RJ (2014). Low-temperature processed electron collection layers of graphene/TiO_2 nanocomposites in thin film perovskite solar cells. Nano Letters, 14, 724–730.

[12] Zhou H, Chen Q, Li G, Luo S, Song T-B, Duan H-S, Hong Z, You J, Liu Y, Yang Y (2014). Interface engineering of highly efficient perovskite solar cells. Science, 345, 542–546.

[13] Jeon NJ, Noh JH, Yang WS, Kim YC, Ryu S, Seo J, Seok SI (2015). Compositional engineering of perovskite materials for high-performance solar cells. Nature, 517, 476–480.

[14] Nie W, Tsai H, Asadpour R, Blancon JC, Neukirch AJ, Gupta G, Crochet JJ, Chhowalla M, Tretiak S, Alam MA, Wang HL, Mohite AD (2015). High-efficiency solution-processed perovskite solar cells with millimeter-scale grains. Science, 347, 522–525.

[15] Yang WS, Noh JH, Jeon NJ, Kim YC, Ryu S, Seo J, Seok SI (2015). High-performance photovoltaic perovskite layers fabricated through intramolecular exchange. Science, 348, 1234–1237.

[16] Saliba M, Orlandi S, Matsui T, Aghazada S, Cavazzini M, Correa-Baena JP, Gao P, Scopelliti R, Mosconi E, Dahmen KH, De Angelis F, Abate A, Hagfeldt A, Pozzi G, Graetzel M, Nazeeruddin MK (2016). A molecularly engineered hole-transporting material for efficient perovskite solar cells. Nature Energy, 1, 15017-1–15017-7.

[17] Bi D, Tress W, Dar MI, Gao P, Luo J, Renevier C, Schenk K, Abate A, Giordano F, Baena JPC, Decoppet JD, Zakeeruddin SM, Nazeeruddin MK, Grätzel M, Hagfeldt A. (2016). Efficient luminescent solar cells based on tailored mixed-cation perovskites. Science Advances, 2, e1501170-1–e1501170-7.

[18] Saliba M, Matsui T, Seo JY, Domanski K, Correa-Baena JP, Nazeeruddin MK, Zakeeruddin SM, Tress W, Abate A, Hagfeldtd A, Grätzel M (2016). Cesium-containing triple cation perovskite solar cells: improved stability, reproducibility and high efficiency. Energy Environmental Science, 9, 1989–1997.

[19] Oku T. Crystal structures of $CH_3NH_3PbI_3$ and related perovskite compounds used for solar cells, in Solar Cells – New Approaches and Reviews, Editor, Kosyachenko LA. Rijeka, Croatia (2015). InTech 77–102.

[20] Oku T, Takeda A, Nagata A, Kidowaki H, Kumada K, Fujimoto K, Suzuki A, Akiyama T, Yamasaki Y, Ōsawa E (2013). Microstructures and photovoltaic properties of C_{60} based solar cells with copper oxides, $CuInS_2$, phthalocyanines, porphyrin, PVK, nanodiamond, germanium and exciton diffusion blocking layers. Materials Technology, 28, 21–39.

[21] Oku T (2012). Direct structure analysis of advanced nanomaterials by high-resolution electron microscopy. Nanotechnology Reviews, 1, 389–425.

[22] Oku T (2014). High-resolution electron microscopy and electron diffraction of perovskite-type superconducting copper oxides. Nanotechnology Reviews, 3, 413–444.

[23] Oku T (2014). Structure analysis of advanced nanomaterials: nanoworld by high-resolution electron microscopy. Walter De Gruyter Inc. Berlin, Germany.

[24] Weber D (1978). $CH_3NH_3PbX_3$, a Pb(II)-system with cubic perovskite structure, Zeitschrift für Naturforschung B, 33, 1443–1445.

[25] Poglitsch A, Weber D (1987). Dynamic disorder in methylammonium trihalogeno-plumbates (II) observed by millimeter-wave spectroscopy. The Journal of Chemical Physics, 87, 6373–6378.

[26] Onoda-Yamamuro N, Matsuo T, Suga H (1990). Calorimetric and IR spectroscopic studies of phase transitions in methylammonium trihalogenoplumbates (II). Journal of Physics and Chemistry of Solids, 51, 1383–1395.

[27] Mashiyama H, Kurihara Y, Azetsu T (1998). Disordered cubic perovskite structure of $CH_3NH_3PbX_3$ (X=Cl, Br, I). Journal of the Korean Physical Society, 32, S156–S158.

[28] Chen T, Benjamin JF, Ipek B, Tyagi M, Copley JRD, Brown CM, Choi JJ, Lee SH (2015). Rotational dynamics of organic cations in the $CH_3NH_3PbI_3$ perovskite. Physical Chemistry Chemical Physics, 17, 31278–31286.

[29] Weller MT, Weber OJ, Frost JM, Walsh A (2015). Cubic perovskite structure of black formamidinium lead iodide, α-[$HC(NH_2)_2$]PbI_3, at 298 K. Journal of Physical Chemistry Letters, 6, 3209–3212.

[30] Yamada K, Funabiki S, Horimoto H, Matsui T, Okuda T, Ichiba S (1991). Structural phase transitions of the polymorphs of $CsSnI_3$ by means of Rietveld analysis of the X-ray diffraction. Chemistry Letters, 20, 801–804.

[31] Chung I, Song JH, Im J, Androulakis J, Malliakas CD, Li H, Freeman AJ, Kenney JT, Kanatzidis MG (2012). $CsSnI_3$: semiconductor or metal? High electrical conductivity and strong near-infrared photoluminescence from a single material. High hole mobility and phase-transitions. Journal of the American Chemical Society, 134, 8579–8587.

[32] Thiele G, Rotter HW, Schmidt KD (1987). Crystal structures and phase transformations of cesium trihalogenogermanates $CsGeX_3$ (X = Cl, Br, I). Zeitschrift für Anorganische und Allgemeine Chemie, 545, 148–156.

[33] Zushi M, Suzuki A, Akiyama T, Oku T (2014). Fabrication and characterization of TiO_2/$CH_3NH_3PbI_3$-based photovoltaic devices. Chemistry Letters, 43, 916–918.

[34] Oku T, Kakuta N, Kobayashi K, Suzuki A, Kikuchi K (2011). Fabrication and characterization of TiO_2-based dye-sensitized solar cells. Progress in Natural Science: Materials International, 21, 122–126.

[35] Oku T, Zushi M, Imanishi Y, Suzuki A, Suzuki K (2014). Microstructures and photovoltaic properties of perovskite-type $CH_3NH_3PbI_3$ compounds. Applied Physics Express, 7, 121601–1–121601–4.

[36] Kawamura Y, Mashiyama H, Hasebe K (2002). Structural study on cubic–tetragonal transition of $CH_3NH_3PbI_3$. Journal of the Physical Society of Japan, 71, 1694–1697.

[37] Baikie T, Fang Y, Kadro JM, Schreyer M, Wei F, Mhaisalkar SG, Grätzel M, Whitec TJ (2013). Synthesis and crystal chemistry of the hybrid perovskite (CH_3NH_3)PbI_3 for solid-state sensitised solar cell applications. Journal of Materials Chemistry A, 1, 5628–5641.

[38]   Li X, Bi D, Yi C, Décoppet JD, Luo J, Zakeeruddin SM, Hagfeldt A, Grätzel M (2016). A vacuum flash–assisted solution process for high-efficiency large-area perovskite solar cells. Science, 353, 58–62.

[39]   Oku T, Matsumoto T, Suzuki A, Suzuki K (2015). Fabrication and characterization of a perovskite-type solar cell with a substrate size of 70 mm. Coatings, 5, 646–655.

[40]   Dong Q, Fang Y, Shao Y, Mulligan P, Qiu J, Cao L, Huang J (2015). Electron-hole diffusion lengths > 175 μm in solution-grown $CH_3NH_3PbI_3$ single crystals. Science, 347, 967–970.

[41]   Oku T, Iwata T, Suzuki A (2015). Effects of niobium addition into TiO_2 layers on $CH_3NH_3PbI_3$-based photovoltaic devices. Chemistry Letters, 44, 1033–1035.

[42]   Miyagi T, Kamei M, Sakaguchi I, Mitsuhashi T, Yamazaki A (2004). Photocatalytic property and deep levels of Nb-doped anatase TiO_2 film grown by metalorganic chemical vapor deposition. Japanese Journal of Applied Physics, 43, 775–776.

[43]   Emeline AV, Furubayashi Y, Zhang X, Jin M, Murakami T, Fujishima A (2005). Photo-electrochemical behavior of Nb-doped TiO_2 electrodes. The Journal of Physical Chemistry B, 109, 24441–24444.

[44]   Hirano M, Matsushima K (2006). Photoactive and adsorptive niobium-doped anatase (TiO_2) nanoparticles: influence of hydrothermal conditions on their morphology, structure, and properties. Journal of the American Ceramic Society, 89, 110–117.

[45]   Zhang SX, Kundaliya DC, Yu W, Dhar S, Young SY, Salamanca-Riba LG, Ogale SB, Vispute RD, Venkatesan T (2007). Niobium doped TiO_2: intrinsic transparent metallic anatase versus highly resistive rutile phase. Journal of Applied Physics, 102, 013701.

[46]   Maghanga CM, Jensen J, Niklasson GA, Granqvist CG, Mwamburi M (2010). Transparent and conducting TiO_2:Nb films made by sputter deposition: application to spectrally selective solar reflectors. Solar Energy Materials and Solar Cells, 94, 75–79.

[47]   Tian Y, Tatsuma T (2005). Mechanisms and applications of plasmon-induced charge separation at TiO_2 films loaded with gold nanoparticles. Journal of the American Chemical Society, 127, 7632–7637.

[48]   Matsumoto T, Oku T, Akiyama T (2013). Incorporation effect of silver nanoparticles on inverted type bulk-heterojunction organic solar cells. Japanese Journal of Applied Physics, 52, 04CR13–1–04CR13–5.

[49]   Oku T, Suzuki K, Suzuki A (2016). Effects of chlorine addition to perovskite-type $CH_3NH_3PbI_3$ photovoltaic devices. Journal of the Ceramic Society of Japan, 124, 234–238.

[50]   Shi D, Adinolfi V, Comin R, Yuan M, Alarousu E, Buin A, Chen Y, Hoogland S, Rothenberger A, Katsiev K, Losovyj Y, Zhang X, Dowben PA, Mohammed OF, Sargent

EH, Bakr OM (2015). Low trap-state density and long carrier diffusion in organolead trihalide perovskite single crystals. Science, 347, 519–522.

[51] Hao F, Stoumpos CC, Cao DH, Chang RPH, Kanatzidis MG (2014). Lead-free solid-state organic-inorganic halide perovskite solar cells. Nature Photonics, 8, 489–494.

[52] Hao F, Stoumpos CC, Guo P, Zhou N, Marks TJ, Chang RPH, Kanatzidis MG (2015). Solvent-mediated crystallization of $CH_3NH_3SnI_3$ films for heterojunction depleted perovskite solar cells. Journal of the American Chemical Society, 137, 11445–11452.

[53] Oku T, Ohishi Y, Suzuki A (2016). Effects of antimony addition to perovskite-type $CH_3NH_3PbI_3$ photovoltaic devices. Chemistry Letters, 45, 134–136.

[54] Oku T, Ohishi Y, Suzuki A, Miyazawa Y (2016). Effects of Cl addition to Sb-doped perovskite-type $CH_3NH_3PbI_3$ photovoltaic devices. Metals, 6, 147–1–147–13.

[55] Krishnamoorthy T, Ding H, Yan C, Leong WL, Baikie T, Zhang Z, Sherburne M, Li S, Asta M, Mathews N, Mhaisalkarac SG (2015). Lead-free germanium iodide perovskite materials for photovoltaic applications. Journal of Materials Chemistry A, 3, 23829–23832.

[56] Ohishi Y, Oku T, Suzuki A (2016). Fabrication and characterization of perovskite-based $CH_3NH_3Pb_{1-x}Ge_xI_3$, $CH_3NH_3Pb_{1-x}Tl_xI_3$ and $CH_3NH_3Pb_{1-x}In_xI_3$ photovoltaic devices. AIP Conference Proceedings, 1709, 020020-1–020020-8.